

## Article

# A Study of a Cryogenic CuAlMn Shape Memory Alloy

Adelaide Nespoli <sup>1,\*</sup>, Francesca Passaretti <sup>1</sup>, Davide Ninarello <sup>1,2</sup>, Marcella Pani <sup>3</sup>, Cristina Artini <sup>3,4</sup>,  
Francesca Ferro <sup>3</sup> and Carlo Fanciulli <sup>1</sup>

<sup>1</sup> National Research Council, Institute of Condensed Matter Chemistry and Technologies for Energy (CNR-ICMATE), Via G. Previati 1/e, 23900 Lecco, Italy; francesca.passaretti@cnr.it (F.P.); davide.ninarello@polimi.it (D.N.); carlo.fanciulli@cnr.it (C.F.)

<sup>2</sup> Department of Chemistry, Materials and Chemical Engineering "Giulio Natta" (CMIC), Politecnico di Milano, Piazza Leonardo da Vinci, 32, 20133 Milano, Italy

<sup>3</sup> Department of Chemistry and Industrial Chemistry (DCCI), University of Genova, Via Dodecaneso 31, 16146 Genova, Italy; marcella@chimica.unige.it (M.P.); artini@chimica.unige.it (C.A.); 4643245@studenti.unige.it (F.F.)

<sup>4</sup> National Research Council, Institute of Condensed Matter Chemistry and Technologies for Energy (CNR-ICMATE), Via De Marini 6, 16149 Genova, Italy

\* Correspondence: adelaide.nespoli@cnr.it; Tel.: +39-0341-2350-116

**Abstract:** In extreme temperature environments, a newly emerging engineering application involves both the active and passive control of structures using cryogenic shape memory alloys, which are smart materials able to recover high deformation below the freezing point. With the objective of carrying out new advances in this area, the present work aims to investigate the Cu-7.5Al-13.5Mn (wt.%) shape memory alloy. Thermal, microstructural, and thermomechanical analyses of as-cast and hot-rolled specimens were performed, taking into account the effects of annealing and solubilization. It was observed that the phase transition occurs at temperatures below 120 K and changes according to the thermo-mechanical path. Specifically, hot-rolling lowers the phase transition temperature range with respect to the as-cast condition—from 34 K to 23 K for  $M_f$ , and from 89 K to 80 K for  $A_f$ . Additionally, when the annealing temperature rises, the phase transformation temperature increases as well, and the alloy loses its cryogenic features when heat treated above 473 K. Finally, loss factors of 0.06 and 0.088, which were respectively found in dynamic and static settings, validate the material's good damping response.

**Keywords:** shape memory alloy; cryogenic; CuAlMn; low temperature



**Citation:** Nespoli, A.; Passaretti, F.; Ninarello, D.; Pani, M.; Artini, C.; Ferro, F.; Fanciulli, C. A Study of a Cryogenic CuAlMn Shape Memory Alloy. *Metals* **2024**, *14*, 323. <https://doi.org/10.3390/met14030323>

Academic Editors: Thomas Niendorf and Ibrahim Karaman

Received: 8 February 2024

Revised: 28 February 2024

Accepted: 9 March 2024

Published: 11 March 2024



**Copyright:** © 2024 by the authors. Licensee MDPI, Basel, Switzerland. This article is an open access article distributed under the terms and conditions of the Creative Commons Attribution (CC BY) license (<https://creativecommons.org/licenses/by/4.0/>).

## 1. Introduction

Shape memory alloys (SMA) are smart materials known for their capability to recover high strains thanks to peculiar properties, such as the shape memory, SME, and pseudoelastic (PE) effects. These two features originate in a reversible thermoelastic transition between two solid phases, austenite and martensite, which are respectively stable at high and low temperatures. The transition between austenite and martensite can either be induced by a change of temperature, as in the case of SME, or by a change of load, as in the case of PE [1]. Furthermore, the phase transition usually involves high strain recovery and the resulting mechanical work is frequently exploited in actuation (SME), to produce motion, and also in passive damping (PE), to damp vibration or absorb impacts [2].

The phase transition of SMA is identified by four characteristic temperatures ( $M_s$ ,  $M_f$ ,  $A_s$  and  $A_f$ ) that are the temperatures at which the austenite-to-martensite (M) and martensite-to-austenite (A) transitions start (s) and finish (f). The temperature range of stability of the two phases is primarily determined by the chemical composition of the alloy and its thermo-mechanical history, which includes mechanical processing and thermal treatments. However, when designing an application, it is important to consider that the martensitic transformation is also affected by other factors, like the environmental

temperature and the applied load (Clausius-Clapeyron law, [3]). As a result, constraints directly related to the target application, such as operating temperature, applied load, deformation range and life cycling, have to drive the designer's choice of the SMA material.

Applications of SMA usually involve NiTi, NiTi-based and Cu-based alloys at a temperature ranging from room temperature (PE) [4,5] to approximately 400 K for typical SME alloys [6], or up to roughly 600 K for high temperature SMA, such as NiTiHf [2].

The Cu-based system has gathered a lot of interest in SMA applications because of its competitive strain recovery, damping qualities, and cost-effectiveness, when compared to the well-known NiTi system [7]. These benefits are however outweighed by additional problems, including their innate brittleness and aging-based martensite stabilization. The Cu-Al-Mn alloys, with low aluminum contents, show an excellent ductility, good workability, an interesting shape memory, and also have pseudoelastic properties [8,9]. Because of the Mn-Mn interaction, the Cu-Al-Mn system is classified as part of the ferromagnetic SMA class of SMA [10]. In these alloys, the coupling of the magnetism and the structure leads to peculiar magneto-mechanical and important functional materials that are characterized by both ferromagnetic behavior and the shape memory property [11–14]. Moreover, it has been shown that transition temperatures, the material's workability, and the kind of martensitic structure are all highly impacted by aging and by changes to the manganese and aluminum content and ratio [15,16]. Kozubski et al. [17] provided a comprehensive analysis of the precipitation process during the heat treatment, and discovered that the CuAlMn decomposes into  $\gamma$ -Cu<sub>9</sub>Al<sub>4</sub>, T-Cu<sub>3</sub>Mn<sub>2</sub>Al and  $\beta$ -Mn when heat treated at temperatures below 723 K. This was discovered when studying the stoichiometric alloy Cu<sub>2.00</sub>Al<sub>1.00</sub>Mn<sub>1.00</sub>. It was also highlighted that the primary driver of the precipitation process is the mobility of Mn atoms. At temperatures higher than 673 K, there is a rapid precipitation of  $\beta$ -Mn; at below 673 K, the mobility of atoms of Mn is considerably lower and the nucleation and growth of  $\gamma$ -Cu<sub>9</sub>Al<sub>4</sub> and T-Cu<sub>3</sub>Mn<sub>2</sub>Al are the origin of the appearance of the Mn-rich regions in the alloy. A coherent precipitation with the formation of GP zones has also been reported for heat treatment at temperatures below 573 K. Furthermore, it has also been pointed out that the precipitation process occurring during heating may perturb the signal during an experimental analysis that involves a heating ramp [17].

The active or passive control of structures at cryogenic temperatures through SMA is a novel and appealing application in severe environments where the temperature might drop extremely low. The space industry may be the main field of application for cryogenic shape memory alloys since they can be used to shield equipment (like satellites) from permanent damage caused by temperature fluctuations brought on by differences in sun irradiation when in orbit [18]. Similarly, these alloys can be used to safeguard cryogenic equipment like infrared detection systems, which are frequently employed in low-temperature environments to increase detection efficiency by reducing background noise interference and dark current detection (these detectors typically operate below 150 K) [19]. Furthermore, cryogenic SMA could be used in expandable habitats, deployable platforms, solar cells and veils on demand, and could also be used in adaptive applications and in situ resource utilization (ISRU) technologies.

In a recent work [20], we reported on state-of-the-art SMA that exhibit the phase transition at cryogenic temperature. Within this family, a class of extreme-cryogenic SMA was defined, which consists of SMA with  $M_s$  below 125 K. This class, with the exception of the NiTiHf alloy investigated by Umale et al. [21], only consists of CuAlMn-based systems. Furthermore, it also pointed out new directions for future research of CuAlMn cryogenic alloy, such as focusing on CuAlMn systems with Mn contents higher than 13 wt.%, and Mn/Al ratio higher than 1.5.

On this basis, the present work aims to provide new advances in the research of the cryogenic phase transition of the CuAlMn system. A study we previously conducted [20] guided this study to the selection of the new nominal composition, which led to the choice of 7.5 and 13.5 wt.% of Al and Mn content, respectively, with a Mn/Al ratio equal to 1.8. Furthermore, the selection of this composition was also guided by the studies of

Zak et al. [22] and Wang et al. [23], who previously investigated CuAlMn systems with a similar composition to those studied here. In their work, they suggested estimating the  $M_s$  temperature by using the following equations [22,23]:

$$M_s(\text{K}) = 1192 - 25.5\text{Al}(\text{wt.}\%) - 73.2\text{Mn}(\text{wt.}\%) \quad (1)$$

$$M_s(\text{K}) = 1890 - 42.1\text{Al}(\text{at.}\%) - 78.0\text{Mn}(\text{at.}\%) \quad (2)$$

These two equations were used to further support the selection of the CuAlMn composition, yielding expected  $M_s$  values of 13 K and 143 K, respectively, for the nominal composition used in this work. Here, the designated material is analyzed to assess the shape memory property under cryogenic temperatures. In particular, the microstructure and the phase transformation temperatures, as a function of the annealing route, are investigated through thermal analyses. A comparison with the literature is then carried out to state the existence of a correlation between the phase transformation temperatures and the explored content of Mn and Al. A comparison is also made to published results derived from solubilized CuAlMn systems that present  $M_s$  lower than 125 K (see Table 1).

**Table 1.** Phase transition temperatures and Mn/Al ratio of solubilized CuAlMn systems. Data are listed in descending order of  $M_s$  (Tech: technique used to assess the chemical composition; AAS: atomic absorbing spectroscopy; WDS: wavelength-dispersive-X-ray spectroscopy; ND: not declared).

Reference	Cu [wt.%]	Al [wt.%]	Mn [wt.%]	$M_s$ [K]	$A_f$ [K]	Mn/Al	Tech.
[24]	79.3	11.3	9.4	120	ND	0.832	ND
[22]	80.1	8	11.9	115	143	1.488	AAS
[25]	76.8	12.5	10.7	108	145	0.856	ND
[22]	79.6	8.4	12	106	137	1.429	AAS
[26]	79.5	8.7	11.8	106	122	1.363	WDS
[26]	78.4	9.4	12.2	98	116	1.299	WDS
[22]	79.1	8.9	12	92	123	1.348	AAS
[11]	79.8	8.5	11.7	82	ND	1.376	ND
[26]	78.4	9.2	12.4	70	91	1.345	WDS

Finally, the pseudoelastic mechanical response of the selected alloy is assessed through the study of the loss factor parameter (also known as  $\tan\delta$ ). The loss factor is a valuable parameter for engineering applications because it provides insight into the absorbing and dissipating properties of a material or a structure. For the scope of this work, the loss factor was evaluated as the ratio between the loss and the stored energy over the entire mechanical cycle [27].

## 2. Materials and Methods

Starting with the pure (>99%) metallic elements, two ingots of CuAlMn with nominal composition of 7.5 Al, 13.5 Mn, Cu bal. (wt.%) were prepared by a non-consumable electrode vacuum arc furnace (Leybold LK6/45). The ingots were melted into a water-cooled copper crucible in a protective atmosphere (pure 99.999 Ar) and remelted five times to improve the chemical homogeneity. The two ingots, weighing approximately 117 g each, were successively melted together to obtain a single cigar-shaped ingot suitable for subsequent hot deformation. The ingot was hot-rolled (HR) at 1123 K to obtain a 0.56 mm thick ribbon. The HR ribbon was solubilized at 1173 K in Argon atmosphere for 1 h (followed by water quench). Subsequently, several thermal treatments, performed in air, were applied to study the influence of the annealing on the microstructure and the related functional response. Table 2 provides a resuming list of the post-process routes that the CuAlMn samples were subjected to.

**Table 2.** Post-process routes applied to the CuAlMn samples (wq: water quench).

Sample	Post Processing Route
AC_S	As-cast and Solubilized at 1173 K for 1 h (wq)
HR	Hot-Rolled
HR_S	Hot-Rolled + Solubilized at 1173 K for 1 h (wq)
HR_S_373	Hot-Rolled + Solubilized + Heat treated at 373 K for 30 min (wq)
HR_S_473	Hot-Rolled + Solubilized + Heat treated at 473 K for 30 min (wq)
HR_S_673	Hot-Rolled + Solubilized + Heat treated at 673 K for 30 min (wq)

An estimation of the chemical composition of the as-cast CuAlMn sample was performed by using an energy dispersive X-ray spectrometer (EDS, INCA ENERGY 200 Oxford Instr., Oxfordshire, UK) connected to a scanning electron microscope (SEM LEO 1430, Carl Zeiss AG, Jena, Germany). The chemical composition was evaluated by averaging the data of six measurements. In addition, microstructural analyses of mechanically polished samples were accomplished through optical microscopy observations (Leitz-ARISTOMET light Microscope, Leica, Solms, Germany) and through a stereomicroscope (Makroskop Wild M420, Leica, Solms, Germany) equipped with a LED light and polarizer. For microscope observations, the specimens were prepared by mechanical grinding before a final polishing step with 1  $\mu\text{m}$  diamond paste. To enhance the visibility of grains, samples were chemically etched with a solution of ferric chloride acid/methanol/hydrochloric acid (2.5 g  $\text{FeCl}_3 \cdot 6\text{H}_2\text{O}$  + 48 mL  $\text{CH}_3\text{OH}$  + 10 mL  $\text{HCl}$ ) for 10 s. The average grain size was determined by the Heyn Lineal Intercept Procedure (ASTM E112-12).

Structural investigation of the samples was performed by X-ray diffraction (XRD) analysis. XRD patterns were collected at room temperature through a PANalytical X' PERT PRO instrument (Malvern, UK) equipped with Ni-filtered  $\text{Cu K}\alpha$  radiation ( $\lambda = 1.5418 \text{ \AA}$ ) and a X'Cellerator detector. XRD experiments were conducted on bulk samples, exploring the  $2\theta$  range between 10 and  $100^\circ$ , with  $2\theta$  steps of  $0.0167^\circ$  and counting times of 240 s per step.

Moreover, the phase transformation temperatures were assessed through different analyses. In the study, 4-point electrical resistance (ER) measurements were accomplished to detect the phase transition at low temperature. Samples a few centimeters long (with 5 mm width) were taped down to approximately 0.5 mm thickness and coupled to the 4 electrical connections through arc welding. ER data were collected in the range from room temperature to 13 K by means of a home-made apparatus controlled by LabVIEW software (version 14, National Instruments, Austin, TX, USA), which mainly consisted of a Lake Shore temperature controller connected to a cryostat (Figure 1) cooled by He compressor, and calibrated diodes thermometers and a Keithley combination nano-voltmeter plus power source for four-probe resistivity measurement. Since the ER samples are similar in size, a comparison between the ER signal of the different samples was accomplished. The resistivity values, on the other hand, are not provided, since they would not provide reliable values in the whole temperature range, as a result of geometrical indetermination associated with difficulties in measuring the electrical connections' distances.

Furthermore, the phase transition temperatures above room temperature and the melting temperature were evaluated through differential scanning calorimetry (DSC) and differential thermal analysis (DTA), respectively. A Q200 (DSC) and Q600 (DTA) of TA instruments were respectively used to assess the phase transformation temperatures in the range from 273 to 673 K (with 10 K/min heating/cooling rate) and the melting temperature from 900 and 1350 K (with 10 K/min heating rate). Furthermore, DTA analysis of the HR\_S sample was accomplished as well, with a test conducted in the range from 523 to 823 K at 5 K/min.

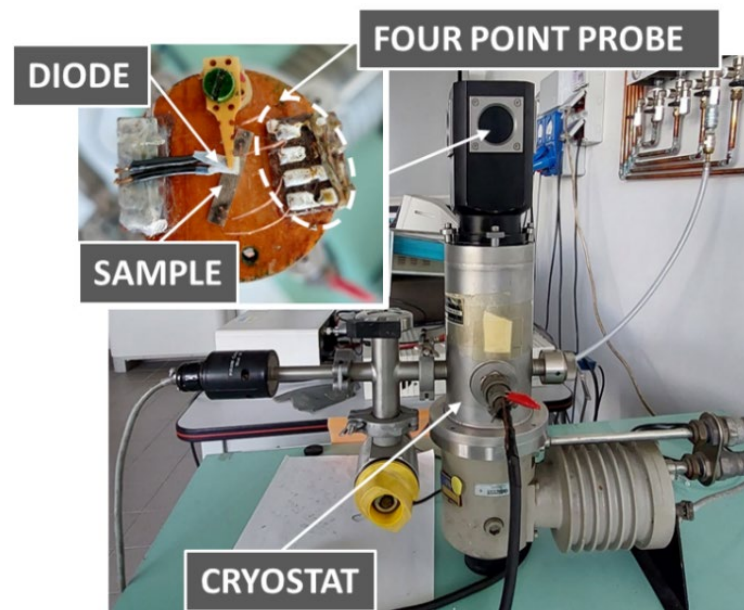


**Figure 1.** Cryostat apparatus used for the 4-point probe electrical measurements.

For ER, DSC and DTA analyses, the characteristic temperatures were identified through the tangent method. The phase transformation temperatures of the CuAlMn alloy examined in this work were compared to those found in the literature, taking into account the alloy composition as well as the Mn/Al ratio.

Finally, three-point bending static and dynamic tests were accomplished through a Q800 TA Instruments testing machine on HR\_S\_473 samples ( $4.5 \times 0.2 \text{ mm}^2$  section). An in-house designed-and-made apparatus composed of two 0.1 mm-radius steel fulcrums placed 10 mm apart, with a centrally placed 0.1 mm-radius steel indenter above them, was firmly installed on the testing stage of the testing machine through a film tension clamp (Figure 2). The instrument was then calibrated for clamp plus apparatus mass, displacement, and compliance, respectively. Static tests were performed at 148 K and 1%/min rate. The loss factor parameter was selected as the key factor to describe the damping behavior of the cryogenic SMA, and was calculated as the ratio between the loss and the stored energy over the entire mechanical cycle, respectively identified by the hysteresis area  $\Delta W$  and  $2\pi W$ , where  $W_{\text{loading}}$  is the loading curve area [27] (see Figure 2). When considering a generic mechanical cycle, the loss factor is calculated as:

$$\text{loss factor} = \frac{\Delta W}{2\pi W_{\text{loading}}} \quad (3)$$

where  $W$  is the mechanical energy stored during the loading path, defined as:

$$W_{\text{loading}} = \int_{x1}^{x2} \sigma_{\text{loading}}(x) S_0 dx \quad (4)$$

and  $\Delta W$  is calculated as:

$$\Delta W = W_{\text{loading}} - \int_{x1}^{x2} \sigma_{\text{unloading}}(x) S_0 dx \quad (5)$$

with  $S_0$  equal to the cross section of the specimen,  $x1 = 0$  and  $x2$  is the maximum displacement.

Finally, dynamic analysis at 0.125 Hz was accomplished at a strain of 2%.

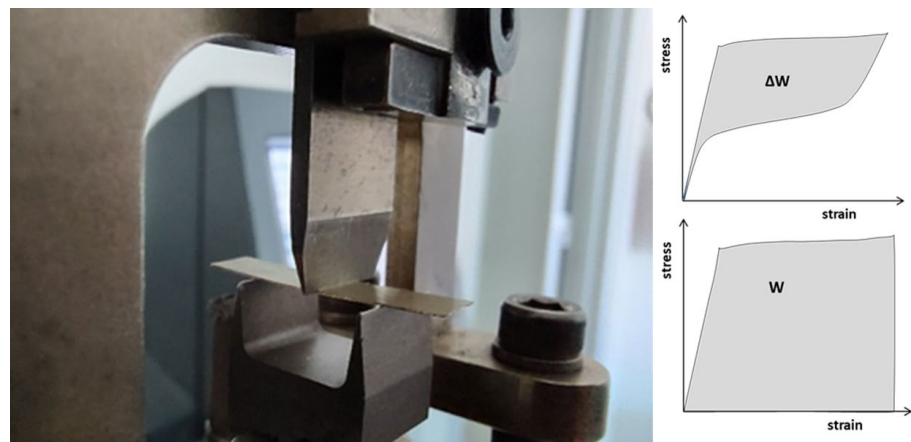


**Figure 2.** Three-point bending apparatus used for the static and dynamic mechanical tests and schematic representation of the energy loss per cycle  $\Delta W$  and the mechanical energy stored during the loading path  $W_{\text{loading}}$ .

### 3. Results

#### 3.1. Microstructure

The optical micrographs of the CuAlMn samples after the steps outlined in Table 1 are shown in Figures 3 and 4. AC, AC\_S, HR, HR\_S, HR\_S\_373 and HR\_S\_473 samples display similar grain morphology, with a single-phase structure and average grain size varying between 0.25 and 0.63 mm (see Figure 5). Analyzing the solubilized samples reveals hot-rolling reduces grain sizes, compared to the specimen as-cast. Furthermore, the average grain size increases with the increases in the temperature of the heat treatment. At room temperature, the grain morphology of the HR\_S\_673 sample differs from that observed for the other specimens, presenting plate-like precipitates that are apparently close to the bainite [15,28] (see Figure 4). According to [28], the formation of bainite should be attributed to the selected thermal treatment temperature. Furthermore, retained martensite was also observed in several grains of the HR specimen, as is clearly visible in the micrographs of Figure 6.

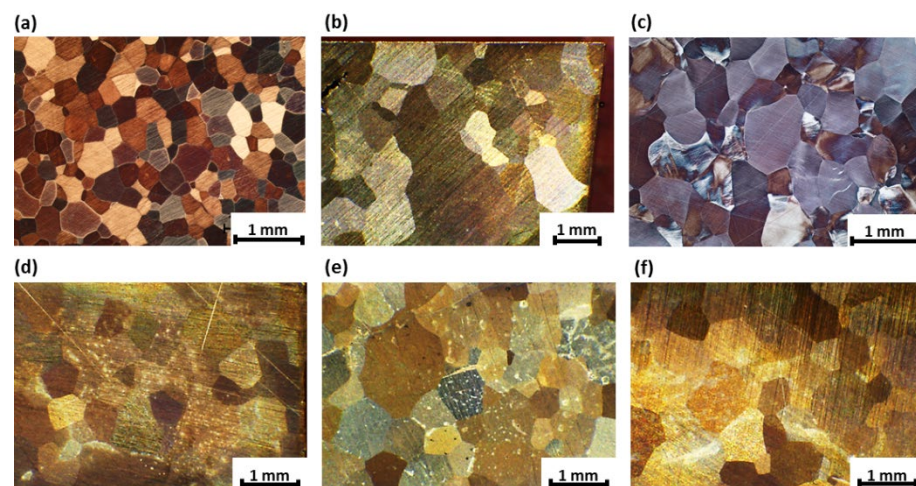


**Figure 3.** Optical microscope images of the etched samples. (a): as-cast sample (AC); (b): solubilized as-cast sample (AC\_S); (c): hot-rolled sample (HR); (d): solubilized hot-rolled sample (HR\_S); (e): solubilized hot-rolled sample heat treated at 373 K (HR\_S\_373); (f): solubilized hot-rolled sample heat treated at 473 K (HR\_S\_473).

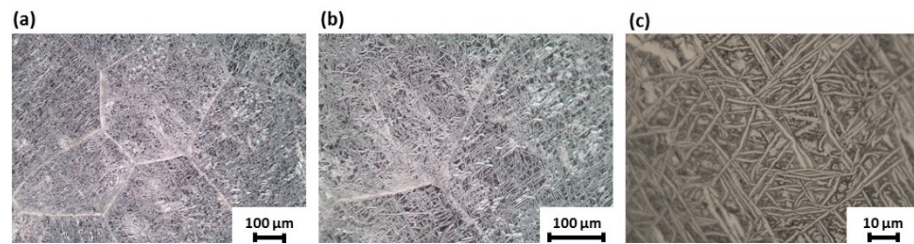


**Figure 4.** Optical microscope images at different magnifications ((a): 100×, (b): 200×, (c): 1000×) of solubilized hot-rolled sample heat treated at 673 K (HR\_S\_673) and chemically etched.

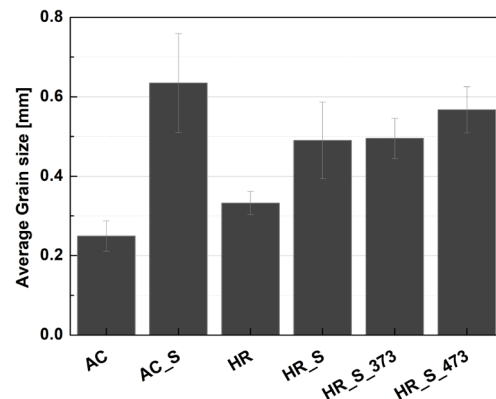


**Figure 5.** Average grain size of CuAlMn samples at different production stages. AC: as-cast sample; AC\_S: solubilized as-cast sample; HR: hot-rolled sample; HR\_S: solubilized hot-rolled sample; HR\_S\_373: solubilized hot-rolled sample heat treated at 373 K; HR\_S\_473: solubilized hot-rolled sample heat treated at 473 K.

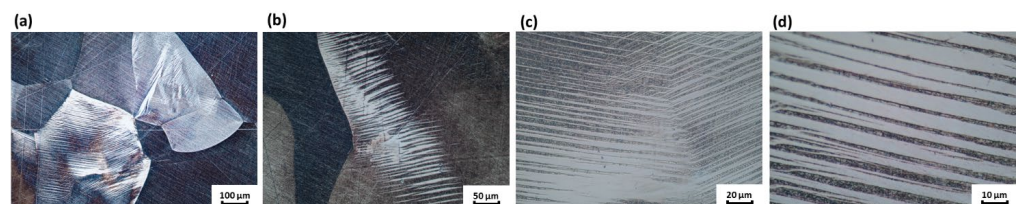


**Figure 6.** Optical microscope images of etched hot-rolled (HR) sample at different magnifications ((a): 100×, (b): 200×, (c): 500×, (d): 1000×).

XRD patterns of the hot-rolled specimens are reported in Figure 7. The peaks of the austenitic phase were identified through comparison with data reported in the Pearson's Crystal Database [29] for the  $Mn_{0.44}Cu_{2.84}Al_{0.72}$  phase ([30],  $Fm\bar{3}m$ ,  $MnCu_2Al$  prototype, L21 structure), which was taken as a reference. Peak intensities are slightly different from sample to sample and do not correspond exactly to those of the reference phase, which may be partly due to the fact that samples were analyzed in bulk and because they underwent a mechanical treatment, meaning a preferential orientation of some reflections is not surprising. In addition to the austenitic phase peaks, which are identified in the figure by the corresponding Miller indices, a further peak is visible in a shoulder of the (220) reflection that has been associated with the martensite phase. From literature data, it is known that while this latter phase crystallizes in a space group of low symmetry (18R monoclinic phase, [31]), no details about unit cell dimensions and crystal structure can be addressed before further analyses. The HR\_S\_673 sample shows a somewhat different situation, which is in accordance with the different microstructure detected by optical microscopy analysis: as shown in Figure 7, several peaks that do not belong to the austenitic phase are present, which are marked with an asterisk and ascribed to the martensite phase.

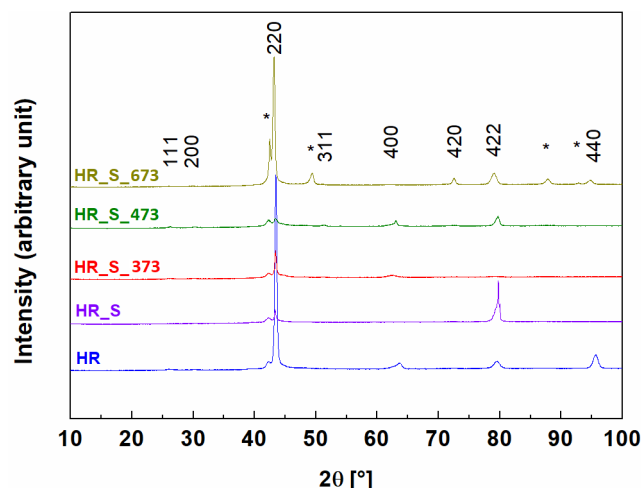


**Figure 7.** Stacked diffractograms of hot-rolled samples; austenite peaks are indexed according to the  $Fm\bar{3}m$  space group, while asterisks mark martensite/extra peaks. HR: hot-rolled sample; HR\_S: hot-rolled and solubilized sample; HR\_S\_373: solubilized hot-rolled samples annealed at 373 K; HR\_S\_473: solubilized hot-rolled sample annealed at 473 K; HR\_S\_673: solubilized hot-rolled samples annealed at 673 K.

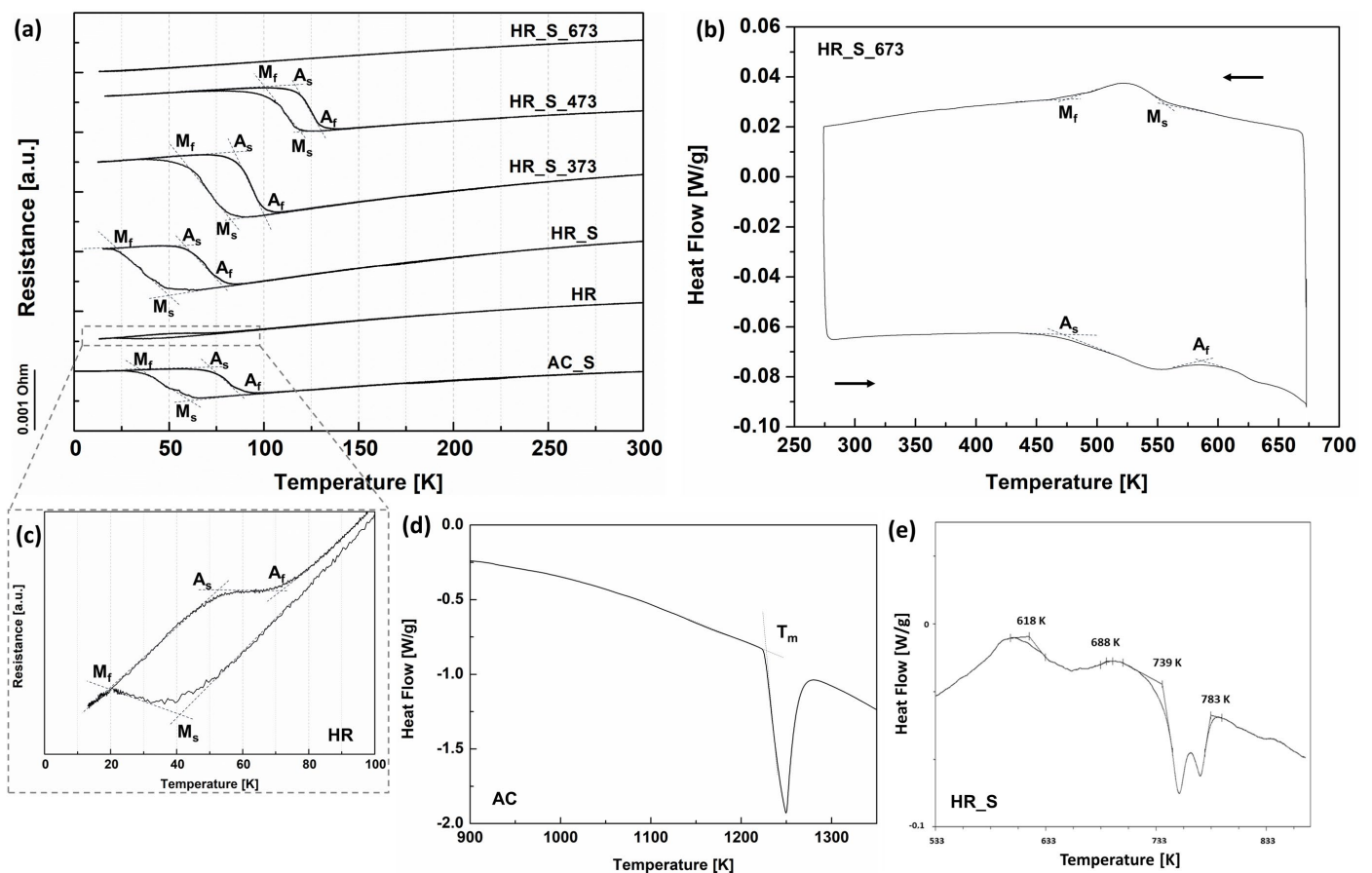
### 3.2. Thermal and Mechanical Analysis

Table 3 reports the estimation of the nominal and the mean measured composition of the cigar-shaped CuAlMn as-cast ingots. It can be noted that the CuAlMn ingot exhibits a chemical composition very close to the nominal one.

**Table 3.** Nominal and mean chemical composition (wt.%) of the CuAlMn ingot (standard deviation in brackets).

wt.%	Cu	Al	Mn
nominal	79	7.5	13.5
measured	79.3 (0.4)	7.4 (0.3)	13.3 (0.5)

Substituting the measured compositional data in empirical Equations (1) and (2), the expected  $M_s$  value of the as-cast CuAlMn alloy is 30 K and 166 K, respectively, somewhat higher than those calculated with the nominal composition. In the current study, the phase transformation temperatures of the CuAlMn specimens were assessed through electrical resistance and differential scanning calorimetry measurements: the corresponding curves are reported in Figure 8a–c, while the phase transformation temperatures derived from the two thermal analyses are listed in Table 4. Comparing the  $M_s$  values of the solubilized samples (AC\_S and HR\_S) with the expected ones, it can be stated that empirical Equations (1) and (2) fail to effectively describe the obtained results, which is mostly likely due to the different ranges of Al and Mn content that the two equations were defined in [20]. The DTA curve depicted in Figure 8d shows that the melting temperature of the studied alloy is approximately equal to 1226 K, showing that the heat treatment at 1173 K is effectively a solubilization process for the alloy being considered. Additionally, two precipitation peaks can be seen at 618–688 K and 739–783 K on the DTA curve of the HR\_S sample (see Figure 8d). As Liu et al. previously reported for the  $Cu_{71}Al_{18}Mn_{11}$  alloy [32], these peaks are respectively ascribed to the formation of bainite- and alpha-phase precipitates. The formation of fine microstructure with plate-like bainite plates for heat-treatment from 473 to 673 K of Cu–Al–Mn alloy was also observed in [15,28].



**Figure 8.** Thermal analysis of the CuAlMn alloy. (a): electrical resistance measurements of solubilized as-cast sample (AC\_S), hot-rolled sample (HR), solubilized hot-rolled sample (HR\_S), solubilized hot-rolled samples annealed at 373 K (HR\_S\_373), solubilized hot-rolled sample annealed at 473 K (HR\_S\_473), solubilized hot-rolled sample annealed at 673 K (HR\_S\_673) samples. (b): differential scanning calorimetry of solubilized hot-rolled samples annealed at 673 K (HR\_S\_673). (c): magnification of the electrical resistance measurement of the HR sample. (d): differential thermal analysis of as-cast (AC) sample. (e): differential thermal analysis of solubilized hot-rolled (HR\_S) sample.  $M_s$  and  $M_f$ : martensite start and finish temperature;  $A_s$  and  $A_f$ : austenite start and finish temperature;  $T_m$ : melting temperature. Arrows indicate the heating and cooling directions.

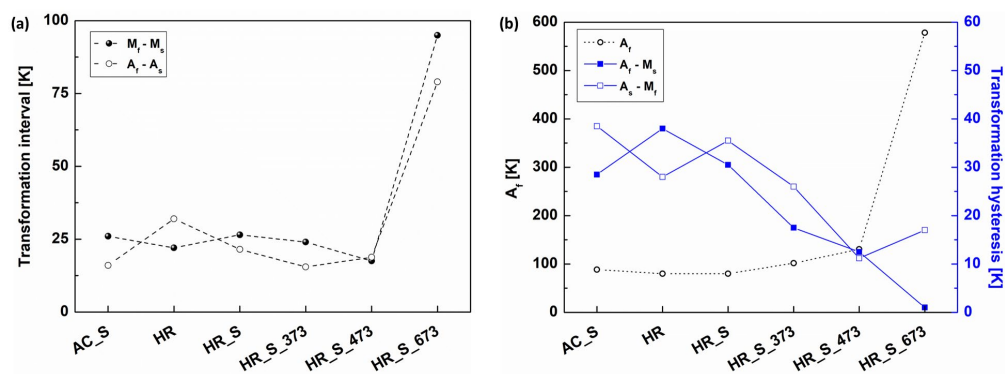
**Table 4.** Phase transformation temperatures of CuAlMn specimens.  $M_s$  and  $M_f$ : martensite start and finish temperatures;  $A_s$  and  $A_f$ : austenite start and finish temperatures; AC\_S: solubilized as-cast; HR: hot-rolled; HR\_S: solubilized hot-rolled; HR\_S\_373: solubilized hot-rolled samples annealed at 373 K; HR\_S\_473: solubilized hot-rolled samples annealed at 473 K; HR\_S\_673: solubilized hot-rolled samples annealed at 673 K.

Sample	$M_s$ [K]	$M_f$ [K]	$A_s$ [K]	$A_f$ [K]
AC_S	60	34	73	89
HR	42	20	48	80
HR_S	50	23	59	80
HR_S_373	84	60	86	102
HR_S_473	118	101	112	131
HR_S_673	577	482	499	578

Table 4 show that hot-rolling lowers the phase transformation temperature range with respect to the as-cast condition, from 34 K to 20 K for  $M_f$  and from 89 K to 80 K for  $A_f$ . On the other hand, the phase transformation temperatures shift to higher values with the

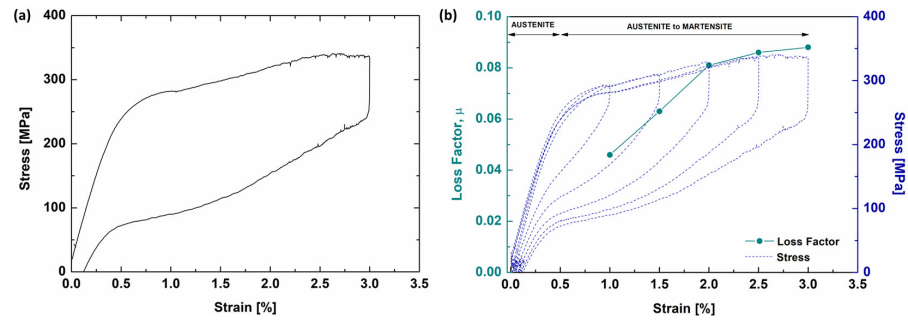
increase of the annealing temperature. Furthermore, it can be observed that the thermal hysteresis of the HR sample is very narrow, allowing an ER signal of martensite very close to that of austenite. It can be observed that no electrical resistance signal was observed for the sample treated at 673 K (HR\_S\_673), which indicates that, at below room temperature, the phase transition is not visible in this sample. DSC was therefore used to determine the phase transformation temperatures for the HR\_S\_673 sample at a temperature higher than the one in the room. By means of differential scanning calorimetry, the HR\_S\_673 sample's phase transformation is identified in a temperature range from 480 to 580 K. Therefore, when treated at 673 K the selected CuAlMn material behaves like a high-temperature material. On the other hand, the alloy exhibits a cryogenic phase transition when annealed at temperatures lower than 473 K.

Figure 9 shows the trends of the transformation intervals ( $M_f - M_s$  and  $A_f - A_s$ ), of  $A_f$ , and of the transformation hysteresses ( $A_f - M_s$  and  $A_s - M_f$ ) with respect to the process route. When the thermal treatment is kept at a temperature at or below 473 K, it can be seen that the transformation intervals are unaffected by the heat treatment temperature (see Figure 9a). In this case the two intervals are very similar and are equal to 23.2 K (with standard deviation of 3.6 K) and 20.8 K (with standard deviation of 6.7 K) for  $M_f - M_s$  and  $A_f - A_s$ , respectively. For higher heat treatment temperatures, the two temperature ranges jump to significantly higher values of 95 K for  $M_f - M_s$  and 79 K for  $A_f - A_s$ . Furthermore, when the temperature of annealing increases,  $A_f$  is seen to move to higher temperatures (see Figure 9b). It approximately changes from 80–90 K (for the as-cast and hot-rolled specimens) to 100–130 K (for the 373–473 K annealed specimens).  $A_f$  rapidly increases to 578 K upon the 673 K thermal treatment, and the transformation hysteresis becomes narrower when the annealing temperature increases.



**Figure 9.** Transformation intervals (a), austenite finish temperature  $A_f$  (b) and transformation hysteresis (b) as a function of the processing route. AC\_S: solubilized as-cast sample; HR: hot-rolled; HR\_S: solubilized hot-rolled sample; HR\_S\_373: solubilized hot-rolled sample heat treated at 373 K; HR\_S\_473: solubilized hot-rolled sample heat treated at 473 K; HR\_S\_673: solubilized hot-rolled sample heat treated at 673 K.

To evaluate the mechanical response of the new CuAlMn system, a loading–unloading study of the HR\_S\_473 sample was conducted. The flag-shaped PE was investigated at 148 K, approximately equal to  $A_f + 15$  K (see Figure 10a). The repetition of the mechanical cycles at different strains enabled the calculation of the loss factor as a function of the advancement of the stress-induced martensite (SIM) transition. The loss factor increases as the SIM transition advances, as can be observed in the graph of Figure 10b, and achieves its highest value when the SIM transition is virtually finished. When SIM transformation is at the beginning, i.e., at 1% strain, the loss factor is at a minimum since the microstructure is mostly austenite. With the progression of transformation into SIM, the loss factor increases until it stabilizes to 0.088. At 0.125 Hz solicitation frequency, the loss factor and the energy loss show a decreasing trend with cycling stabilizing, respectively, to approximately 0.06 and 2 mJ at cycle 10th, as reported in Figure 11.



**Figure 10.** Three-point bending analysis at 148 K of the solubilized hot-rolled sample annealed at 473 K (HR\_S\_473). (a): stress vs. strain at 3%; (b): loss factor  $\mu$  as a function of the applied strain superimposed on the stress vs. strain curves taken for different strains.

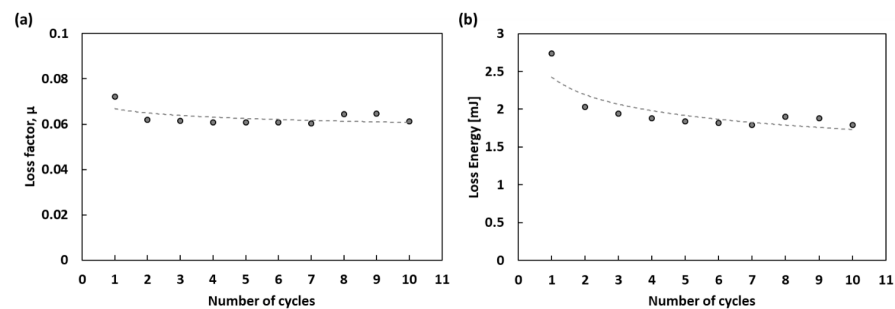


**Figure 11.** Data points (with dashed line as a guide to the eye) of the loss factor, (a), and loss energy, (b), as a function of the mechanical cycle. Test was accomplished on the solubilized hot-rolled sample annealed at 473 K (HR\_S\_200) at 148 K, 2% strain and 0.125 Hz.

#### 4. Discussion

This work constitutes an initial step toward novel understandings of shape memory alloys' cryogenic applications. The CuAlMn system with 7.5 Al, 13.5 Mn and Cu bal. (wt.%) was investigated for this purpose.

The Mn/Al ratio and  $M_s$  temperature of the solubilized CuAlMn samples obtained in the current study are compared with those we collected in a previous work [20] (see Figure 12). Even though the investigations employed different techniques to ascertain the chemical composition (as reported in Table 1), a distinct trend in the  $M_s$  temperature can be seen. A linear decreasing trend of  $M_s$  with Mn content (Figure 12a) can particularly be noted. It is also important to note that, when compared to the composition previously examined by other researchers, the CuAlMn alloy investigated there has the lowest  $M_s$  temperature (50 K for HR\_S and 60 K for AC\_S), which can be attributed to the alloy's highest Mn content (13.3 wt.%) and Mn/Al weight ratio (1.8). This suggests that higher Mn content and Mn/Al ratio may contribute to further decreases of transition temperatures.

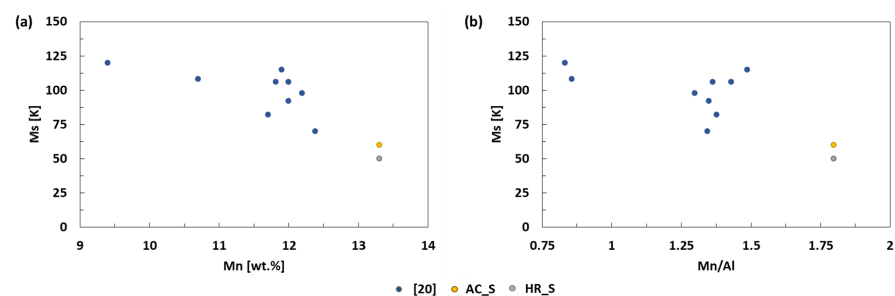


**Figure 12.** Phase transformation temperature  $M_s$  as a function of Mn content, (a), and of Mn/Al ratio, (b). AC\_S: solubilized as-cast sample (yellow dot); HR\_S: solubilized hot-rolled sample (grey dot). Blue dots: solubilized CuAlMn samples from the literature [20].

Furthermore, it was observed that the heat treatments change the phase transition temperatures of the CuAlMn alloy. When the annealing temperature rises, the phase transformation temperatures increase as well, and the alloy loses its cryogenic features when heat treated above 473 K. Considering the  $M_f$  temperature, the 373 K and 473 K heat treatments produce and increase  $M_f$  of approximately 40 K and 80 K, respectively. After the 673 K heat treatment the  $M_f$  increases by approximately 460 K, which can be ascribed to a significant change of the microstructure. The DTA study performed on the HR\_S sample (Figure 8e) confirms that bainite precipitates at 673 K. The notable modifications in the material thermal reactivity (Figure 9) is therefore ascribed to bainite formation. Moreover, Kožuh et al. [33] pointed out that precipitation in CuAlMn produces a change in the chemical composition of the matrix. Indeed, it has been found that the CuAlMn alloy's phase transition temperatures are highly dependent on composition [34]. As a result, the bainite formation is responsible for the observed increase in phase transformation temperatures and the loss of the cryogenic feature.

Finally, loss factors of 0.06 and 0.088 were respectively found in dynamic and static settings. In [35] it is reported that, among the traditional materials prepared from bulk, gray cast iron presents a high loss factor (0.028), which is principally attributed to the presence of graphite that absorbs the energy and converts it into heat. Furthermore, of hybrid materials, aluminum foams and corrugated sandwich components represent an innovative category of lightweight materials with a relatively high loss factor (0.01). Similar results were found for manganese alloys. Therefore, when compared with traditional materials, the CuAlMn alloy investigated here presents a higher damping response. In conclusion, the work highlights encouraging results that deserve further in-depth examinations.

## 5. Conclusions

This work, in presenting new achievements related to cryogenic shape memory alloys, will help to advance the study of the CuAlMn system. It was observed that Mn content higher than 13 wt.% and Mn/Al weight ratio higher than 1.5 are beneficial for attaining phase transformation temperatures lower than 90 K. Furthermore, a linear trend between  $M_s$  and Mn content was confirmed.

When heat treated at 673 K, the microstructure and thermal characteristics of the material exhibits notable changes, to the point where it no longer behaves like a cryogenic material. The pseudoelastic and the shape memory effect take place at a cryogenic temperature, when the temperature of the 30-min heat treatment is kept at or below 473 K.

Finally, mechanical tests at 148 K of the sample annealed at 473 K show a loss factor index that stabilizes to 0.088 and 0.06 in static and dynamic configuration, respectively, confirming a good damping response of the CuAlMn system.

**Author Contributions:** Conceptualization, A.N.; data curation, A.N.; formal analysis, A.N., M.P., F.F. and D.N.; investigation, A.N., M.P., F.F. and C.F.; methodology, A.N., M.P., C.A. and C.F.; resources, F.P.; supervision, A.N.; validation, A.N., M.P., F.F. and C.F.; visualization, A.N.; writing—original draft, A.N.; writing—review & editing, A.N., F.P., M.P., C.A., F.F., C.F. and D.N. All authors have read and agreed to the published version of the manuscript.

**Funding:** This research received no external funding.

**Data Availability Statement:** The original contributions presented in the study are included in the article, further inquiries can be directed to the corresponding author.

**Acknowledgments:** The authors would like to express their gratitude to Enrico Bassani and Nicola Bennato for their technical support.

**Conflicts of Interest:** The authors declare no conflicts of interest.

## References

1. Duerig, T.W.; Melton, K.N.; Stockel, D.; Wayman, C.M. *Engineering Aspects of Shape Memory Alloys*; Elsevier Ltd.: Amsterdam, The Netherlands; Butterworth–Heinemann: Oxford, UK, 1990. [[CrossRef](#)]
2. Concilio, A.; Antonucci, V.; Auricchio, F.; Lecce, L.; Sacco, E. *Shape Memory Alloy Engineering for Aerospace, Structural and Biomedical Applications*; Elsevier Ltd.: Amsterdam, The Netherlands; Butterworth–Heinemann: Oxford, UK, 2021. [[CrossRef](#)]
3. Otsuka, K.; Ren, X. Physical metallurgy of Ti–Ni-based shape memory alloys. *Prog. Mater. Sci.* **2005**, *50*, 511–678. [[CrossRef](#)]
4. Patel, S.K.; Behera, B.; Swain, B.; Roshan, R.; Sahoo, D.; Behera, A. A review on NiTi alloys for biomedical applications and their biocompatibility. *Mater. Today Proc.* **2020**, *33*, 5548–5551. [[CrossRef](#)]
5. Nespoli, A.; Dallolio, V.; Villa, E.; Passaretti, F. A new design of a Nitinol ring-like wire for suturing in deep surgical field. *Mater. Sci. Eng. C* **2015**, *56*, 30–36. [[CrossRef](#)]
6. Kim, M.S.; Heo, J.K.; Rodrigue, H.; Lee, H.T.; Pané, S.; Han, M.W.; Ahn, S.H. Shape Memory Alloy (SMA) Actuators: The Role of Material, Form, and Scaling Effects. *Adv. Mater.* **2023**, *35*, 2208517. [[CrossRef](#)]
7. Alaneme, K.K.; Okotete, E.A. Reconciling viability and cost-effective shape memory alloy options—A review of copper and iron based shape memory metallic systems. *Eng. Sci. Technol. Int. J.* **2016**, *19*, 1582–1592. [[CrossRef](#)]
8. Sutou, Y.; Omori, T.; Kainuma, R.; Ishida, K. Ductile Cu–Al–Mn based shape memory alloys: General properties and applications. *Mater. Sci. Technol.* **2008**, *24*, 896–901. [[CrossRef](#)]
9. Liu, J.-L.; Chen, Z.H.; Huang, H.-Y.; Xie, J.-X. Microstructure and superelasticity control by rolling and heat treatment in columnar-grained Cu–Al–Mn shape memory alloy. *Mater. Sci. Eng. A* **2017**, *696*, 315–322. [[CrossRef](#)]
10. Sasmaz, M.; Bayri, A.; Aydogdu, Y. The Magnetic Behavior and Physical Characterization of Cu–Mn–Al Ferromagnetic Shape Memory Alloy. *J. Supercond. Nov. Magn.* **2011**, *24*, 757–762. [[CrossRef](#)]
11. Prado, M.O.; Lovey, F.C.; Civale, L. Magnetic properties of Cu–Mn–Al alloys with shape memory effect. *Acta Mater.* **1998**, *46*, 137–147. [[CrossRef](#)]
12. Cesari, E.; Pons, J.; Santamarta, R.; Segui, C.; Chernenko, V.A. Ferromagnetic shape memory alloys: An overview. *Arch. Metall. Mater.* **2004**, *49*, 779–789.
13. Lázpita, P.; Villa, E.; Villa, F.; Chernenko, V.A. Temperature Dependent Stress–Strain behavior and Martensite Stabilization in Magnetic Shape Memory Ni<sub>51.1</sub>Fe<sub>16.4</sub>Ga<sub>26.3</sub>Co<sub>6.2</sub>. *Metals* **2021**, *11*, 920. [[CrossRef](#)]
14. Villa, E.; Villa, F.; Rodriguez Crespo, B.; Lazpita, P.; Salazar, D.; Chernenko, V.A.; Hosoda, H. Shape memory and elastocaloric properties of melt-spun NiMn-based Heusler alloys. *J. Alloys Compd.* **2023**, *965*, 171437. [[CrossRef](#)]
15. Alaneme, K.K.; Anaele, J.U.; Okotete, E.A. Martensite aging phenomena in Cu-based alloys: Effects on structural transformation, mechanical and shape memory properties: A critical review. *Sci. Afr.* **2021**, *12*, e00760. [[CrossRef](#)]
16. Mallik, U.S.; Sampath, V. Effect of composition and ageing on damping characteristics of Cu–Al–Mn shape memory alloys. *Mater. Sci. Eng. A* **2008**, *478*, 48–55. [[CrossRef](#)]
17. Kozubuski, R.; Soltys, J. Precipitation from metastable  $\beta$ -phase in the Heusler alloy Cu<sub>2.00</sub>Al<sub>1.00</sub>Mn<sub>1.00</sub>. *J. Mater. Sci.* **1983**, *18*, 1689–1697. [[CrossRef](#)]
18. Gordo, P.; Frederico, T.; Melicio, R.; Amorim, A. Implementation of a Cryogenic Facility for Space Debris Analysis. *Appl. Sci.* **2021**, *11*, 948. [[CrossRef](#)]
19. Han, Y.; Zhang, A. Cryogenic technology for infrared detection in space. *Sci. Rep.* **2022**, *12*, 2349. [[CrossRef](#)]
20. Nespoli, A.; Ninarello, D.; Fanciulli, C. A Review on Shape Memory Alloys with Martensitic Transition at Cryogenic Temperatures. *Metals* **2023**, *13*, 1311. [[CrossRef](#)]
21. Umale, T.; Salas, D.; Tomes, B.; Arroyave, R.; Karaman, I. The effects of wide range of compositional changes on the martensitic transformation characteristics of NiTiHf shape memory alloys. *Scr. Mater.* **2019**, *161*, 78–83. [[CrossRef](#)]
22. Zak, G.; Kneissl, A.C.; Zatulskij, G. Shape memory effect in cryogenic Cu–Al–Mn alloys. *Scripta Mater.* **1996**, *34*, 363–367. [[CrossRef](#)]
23. Wang, H.; Huang, H.Y.; Su, Y.J. Tuning the operation temperature window of the elastocaloric effect in Cu–Al–Mn shape memory alloys by composition design. *J. Alloys Compd.* **2020**, *828*, 154265. [[CrossRef](#)]
24. Lei, Y.; Qin, X.; Wan, F.; Liu, P.; Chen, L.; Wang, J. In-situ observation of martensitic transformation in Cu–Al–Mn cryogenic shape memory alloys. *Fusion Eng. Des.* **2017**, *125*, 603–607. [[CrossRef](#)]
25. Bian, Z.; Song, J.; Liu, P.; Wan, F.; Lei, Y.; Wang, Q.; Yang, S.; Zhan, Q.; Chen, L.; Wang, J. In Situ Observation of Thermoelastic Martensitic Transformation of Cu–Al–Mn Cryogenic Shape Memory Alloy with Compressive Stress. *Materials* **2022**, *15*, 3794. [[CrossRef](#)] [[PubMed](#)]
26. Trehern, W.; Ozcan, H.; Franco, B.; Hite, N.; Malone, N.; Loveall, B.; Morrison, T.D.; Benafan, O.; Karaman, I. Exploring thermomechanical functionality of CuAlMn as an extreme low temperature shape memory alloys. *Mater. Lett.* **2022**, *308*, 131246. [[CrossRef](#)]
27. Nespoli, A.; Bassani, E.; Della Torre, D.; Donnini, R.; Villa, E.; Passaretti, F. An experimental study on pseudoelasticity of a NiTi-based damper for civil applications. *Smart Mater. Struct.* **2017**, *26*, 105041. [[CrossRef](#)]
28. Sutou, Y.; Koeda, N.; Omori, T.; Kainuma, R.; Ishida, K. Effects of ageing on bainitic and thermally induced martensitic transformations in ductile Cu–Al–Mn-based shape memory alloys. *Acta Mater.* **2009**, *57*, 5748–5758. [[CrossRef](#)]
29. Villars, P.; Cenzual, K. *Pearson’s Crystal Data: Crystal Structure Database for Inorganic Compounds*; ASM International: Materials Park, OH, USA, 2007.

30. Chatterjee, S.; Chattopadhyay, S.; Giri, S.; Majumdar, S. Nature of the glassy magnetic state in the Cu<sub>2.84</sub>Mn<sub>0.44</sub>Al<sub>0.72</sub> shape memory alloy. *Europhys. Lett.* **2013**, *104*, 47014. [[CrossRef](#)]
31. Niitsu, K.; Kimura, Y.; Omori, T.; Kainuma, R. Cryogenic superelasticity with large elastocaloric effect. *NPG Asia Mater.* **2018**, *10*, e457. [[CrossRef](#)]
32. Liu, J.-L.; Huang, H.-Y.; Xie, J.-X. Effects of aging treatment on the microstructure and superelasticity of columnar-grained Cu<sub>71</sub>Al<sub>18</sub>Mn<sub>11</sub> shape memory alloy. *Int. J. Miner. Metal. Mater.* **2016**, *23*, 1157. [[CrossRef](#)]
33. Kožuh, S.; Gojić, M.; Ivanić, I.; Holjevac Grgurić, T.; Kosec, B.; Anžel, I. The Effect of Heat Treatment on the Microstructure and Mechanical Properties of Cu-Al-Mn Shape Memory Alloy. *Kem. Ind.* **2018**, *67*, 11–17. [[CrossRef](#)]
34. Aksu Canbay, C.; Karagoz, Z.; Yakuphanoglu, F. Controlling of Transformation Temperatures of Cu-Al-Mn Shape Memory Alloys by Chemical Composition. *Acta Phys. Pol. A* **2014**, *125*, 1163–1166. [[CrossRef](#)]
35. Nespoli, A.; Bettini, P.; Villa, E.; Sala, G.; Passaretti, F.; Grande, A.M. A study on damping property of NiTi elements produced by selective laser-beam melting. *Adv. Eng. Mater.* **2021**, *23*, 2001246. [[CrossRef](#)]

**Disclaimer/Publisher’s Note:** The statements, opinions and data contained in all publications are solely those of the individual author(s) and contributor(s) and not of MDPI and/or the editor(s). MDPI and/or the editor(s) disclaim responsibility for any injury to people or property resulting from any ideas, methods, instructions or products referred to in the content.